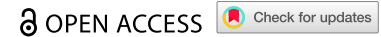


RESEARCH PAPER



Establishment of a visualized mouse orthotopic xenograft model of nasopharyngeal carcinoma

Wei Chen^{a,b}, Wei-Min Chen^a, Si-Xia Chen^a, Li Jiang^{a,b}, Ge-Ge Shu^{b,c}, Yuan-Xiu Yin^{a,b}, Zhi-Peng Quan^{b,c}, Zi-Yan Zhou^{a,b}, Ming-Jun Shen^a, Ya-Ting Qin^a, Chao-Lin Yang^a, Xue-Jin Su^{a,b}, and Min Kang^{a,b}

^aDepartment of Radiation Oncology, The First Affiliated Hospital of Guangxi Medical University, Nanning, Guangxi, China; ^bMinistry of Education, Key Laboratory of Early Prevention and Treatment for Regional High Frequency Tumor (Guangxi Medical University), Nanning, Guangxi, China;

^cDepartment of Hepatobiliary Surgery, The First Affiliated Hospital of Guangxi Medical University, Nanning, Guangxi, China

ABSTRACT

Mouse orthotopic xenograft tumor models are commonly employed in studies investigating the mechanisms underlying the development and progression of tumors and their preclinical treatment. However, the unavailability of mature and visualized orthotopic xenograft models of nasopharyngeal carcinoma limits the development of treatment strategies for this cancer. The aim of this study was to provide a simple and reliable method for building an orthotopic xenograft model of nasopharyngeal carcinoma. Human nasopharyngeal carcinoma (C666-1-luc) cells, stably expressing the firefly luciferase gene, were injected subcutaneously into the right axilla of BALB/C nude mice. Four weeks later, the resulting subcutaneous tumors were cut into small blocks and grafted into the nasopharynx of immunodeficient BALB/C nude mice to induce tumor formation. Tumor growth was monitored by bioluminescence imaging and small animal magnetic resonance imaging (MRI). The expression of histological and immunological antigens associated with orthotopic xenograft nasopharyngeal carcinoma was analyzed by tissue section analysis and immunohistochemistry (IHC). A visualized orthotopic xenograft nasopharyngeal carcinoma model was successfully developed in this study. Luminescence signal detection, micro-MRI, and hematoxylin and eosin staining revealed the successful growth of tumors in the nasopharynx of the nude mice. Moreover, IHC analysis detected cytokeratin (CK), CK5/6, P40, and P63 expression in the orthotopic tumors, consistent with the reported expression of these antigens in human nasopharyngeal tumors. This study established a reproducible, visual, and less lethal orthotopic xenograft model of nasopharyngeal carcinoma, providing a platform for preclinical research.

ARTICLE HISTORY

Received 20 July 2023

Revised 30 May 2024

Accepted 16 July 2024

KEYWORDS



Nasopharyngeal carcinoma; mouse tumor model; orthotopic xenograft model; tissue block; *in vivo* imaging

Introduction

Nasopharyngeal carcinoma, one of the most common types of head and neck tumors, is a squamous cell carcinoma originating from the epithelium of the nasopharynx and primarily located in the roof and anterior wall of the nasopharynx and the Rosenmuller fossa.^{1,2} Globally, approximately 133,000 new cases of nasopharyngeal carcinoma were diagnosed in 2020. However, this cancer is mainly concentrated in North Africa, Southeast Asia, and East Asia, especially China. The global age-standardized rate of nasopharyngeal carcinoma was 16/100,000, whereas that in the high-incidence areas of Southern China was 20–50/100,000.^{1–5}

The World Health Organization classifies nasopharyngeal carcinoma into three histological types: keratinizing squamous cell carcinoma (Type I), non-keratinizing squamous cell carcinoma, and basaloid squamous cell carcinoma; non-keratinizing nasopharyngeal carcinoma is further divided into differentiated (Type II) and undifferentiated (Type III) types.^{1,6,7} In epidemic areas, the majority (>95%) of the nasopharyngeal carcinomas belong to the Type III category and are generally related to Epstein – Barr virus (EBv) infections.^{1,8,9}

Nasopharyngeal cancer is highly sensitive to radiation, with radiotherapy (RT) currently considered the most effective treatment modality.^{10,11} The 5-year overall survival (OS) rates for patients with Stage I or II nasopharyngeal cancer are high, reaching 98% and 92%, respectively.^{7,12} However, the prognosis of patients with Stage III – IVA is poor, with the 5-year OS and progression-free survival of patients undergoing concurrent chemoradiotherapy reported as 70.4% and 61.1%, respectively.¹³ Local recurrence and distant metastasis are the primary causes of treatment failure in nasopharyngeal carcinoma.¹⁴ The emergence of intensity-modulated radiotherapy (IMRT) provides a more conformal dose distribution that releases the concentration of the radiation dose in the target area, while reducing the dose in the surrounding normal tissues, thus significantly improving the treatment outcome of nasopharyngeal carcinoma and reducing off-target adverse events associated with radiotherapy.^{15, 16} However, 5%–10% of patients with this carcinoma experience local recurrence following treatment, and 10%–30% of patients have distant metastasis. Therefore, it is necessary to formulate individualized and precise systemic treatment plans according to the patient's stage and sensitivity to treatment.

CONTACT Min Kang  kangmin@gxmu.edu.cn  Department of Radiation Oncology, The First Affiliated Hospital of Guangxi Medical University, 6 Shuangyong Road, Nanning 530021, China

Wei Chen, Wei-min Chen and Si-xia Chen contributed equally to this work as Co-first author.

© 2024 The Author(s). Published with license by Taylor & Francis Group, LLC.

This is an Open Access article distributed under the terms of the Creative Commons Attribution-NonCommercial License (<http://creativecommons.org/licenses/by-nc/4.0/>), which permits unrestricted non-commercial use, distribution, and reproduction in any medium, provided the original work is properly cited. The terms on which this article has been published allow the posting of the Accepted Manuscript in a repository by the author(s) or with their consent.

Although animal models have proven instrumental in the investigation of various cancer types, a satisfactory model for nasopharyngeal carcinoma is currently lacking. An ideal animal model should mimic the characteristics of the human disease as much as possible and exhibit a high success rate and reproducibility to facilitate the accurate analysis of the disease. Currently, the subcutaneous xenograft model is the most commonly employed animal model of nasopharyngeal carcinoma.^{17–19} Although this model is readily established with a low associated cost and high tumor formation rate, it has some disadvantages. The tumors readily form a capsule, develop locally at the site of injection, and rarely metastasize, thus restricting the ability to mimic the common characteristics of nasopharyngeal carcinoma, which tends to be highly aggressive and commonly metastasizes to the liver, lungs, and bones.^{20,21} Furthermore, xenograft tumors are prone to central necrosis, which is inconsistent with the clinical manifestations of the disease.^{22,23} As an alternative, an orthotopic xenograft model refers to the implantation of human tumor cells into the organ of the animal where the disease originates to simulate the clinical pathogenesis of the tumor. This model can simulate interactions between the actual human tumor and the microenvironment of the interstitium surrounding the organ.^{24,25} Cancer cell differentiation and morphology reflect “active” tumor biological behaviors, including invasion of the surrounding tissues and organs and distant metastasis, while exhibiting similar treatment sensitivity in clinical settings.²⁶

The orthotopic xenograft model is commonly used for studying the biological behaviors and treatment mechanisms of tumors.²⁷ It has been widely applied to investigate the development, progression, and treatment of various tumors in pre-clinical research.^{28,29} Although the application of orthotopic xenograft tumor models at other sites, such as the liver,³⁰ prostate,³¹ and bladder,³² is well established, very few studies report their application in nasopharyngeal carcinoma. Therefore, the primary aim of the current study was to design a murine orthotopic xenograft model of nasopharyngeal carcinoma with high reproducibility that accurately mimics the characteristics of metastasis for wide application in basic and clinical research.

Results

High luciferase gene expression in C666–1-luc cells

First, we screened the lentiviral vector C666–1 tumor cells carrying the firefly luciferase gene with puromycin several times, which grew steadily when the concentration of puromycin reached 3 $\mu\text{g}/\text{mL}$. This cell line was designated the C666–1-luc cell line. RT-qPCR was used to analyze the expression of the luciferase gene in C666–1 cells infected with the virus. The results showed significantly high luciferase gene expression in C666–1-luc cells infected by lentivirus ($p < .0001$; Figure 1a).

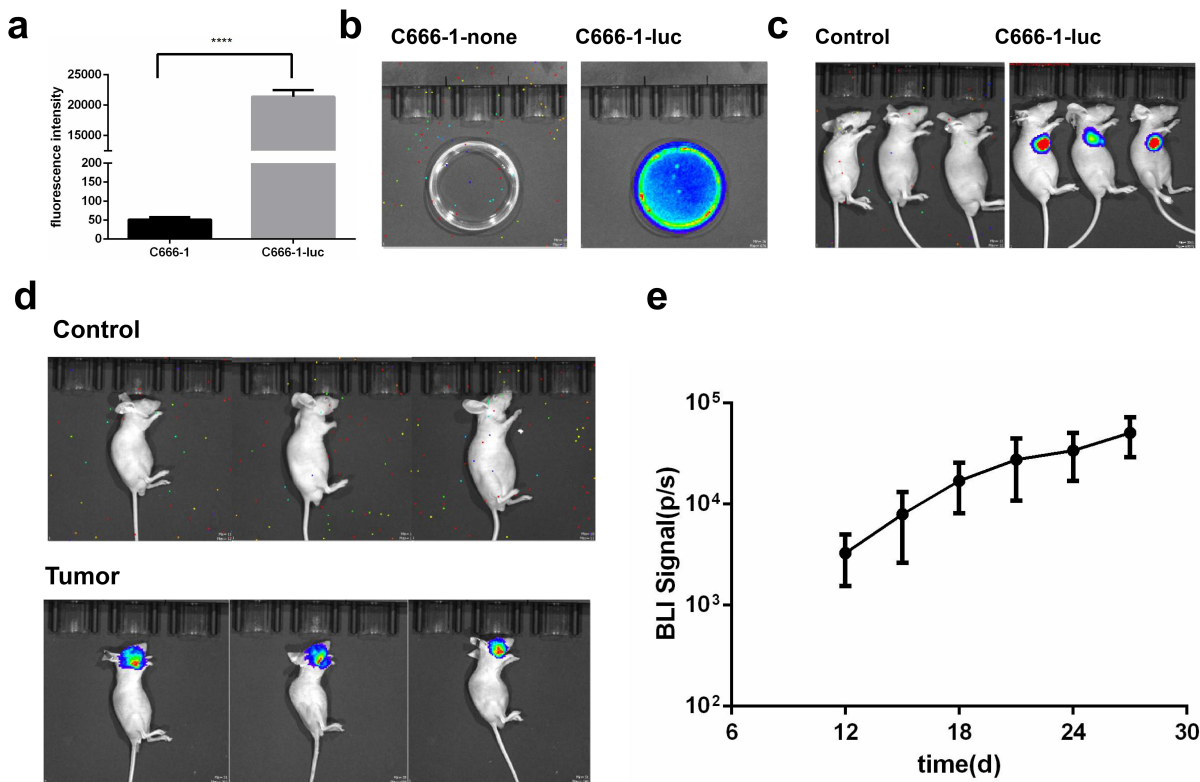


Figure 1. Establishment of the mouse orthotopic xenograft model of nasopharyngeal carcinoma. (a) the overexpression of luciferase in C666-luc cells was assessed at the mRNA level by RT-qPCR (mean \pm SD). Student's t-test, $*p < .0001$. (b) Comparison of the luminescence intensity between C666–1 and C666–1-luc cells. (c) Comparison of the luminescence intensity between mice injected with C666–1 cells and those injected with C666–1-luc cells. (d) The orthotopic xenograft cancer model was observed using the small animal *in vivo* imaging system. Control: images of normal mice. Tumor: mice with nasopharyngeal carcinoma orthotopic xenograft model group. (e) Longitudinal quantification of nasopharyngeal carcinoma bioluminescence imaging (BLI) signals of images obtained at various times (mean \pm SD).

Significant luminescence in C666-1-luc cells *in vitro* and *in vivo*

C666-1 and C666-1-luc cells were imaged *in vitro* and *in vivo*. In the *in vitro* experiments, a significant hyperintense luminescence area was seen in the C666-1-luc cells, but not the C666-1 cells (Figure 1b). Three weeks after the subcutaneous injection of C666-1-luc cells into the axilla, mice bearing subcutaneous tumors were imaged *in vivo*. The subcutaneous tumor areas exhibited a significant hyperintense area, similar in size to that of the subcutaneous tumor (Figure 1c).

Successful establishment of the orthotopic xenograft nasopharyngeal carcinoma Model

Tissue blocks of C666-1-luc cells expressing luciferase after subcutaneous tumor formation were implanted into the nasopharynx of nude mice to establish an orthotopic xenograft nasopharyngeal carcinoma model. The nude mice were scanned on an IVIS Lumina XRMS Serie III imaging system 1 week post-surgery for 5 weeks.

After the tumor was grafted into the nasopharynx of the nude mice, bioluminescence imaging (BLI) revealed a strong and stable high luminescence intensity in the tumor area within the nasopharynx. The hyperintense area representing the tumor increased with time, indicating its growth in the nasopharynx of the nude mice (Figure 1d). Further longitudinal quantification of nasopharyngeal cancer BLI signals obtained through region of interest (ROI) analysis at different time points. The result indicated that the BLI signal of nasopharyngeal carcinoma increased over time, suggesting continuous tumor growth (Figure 1e). A total of 40 mice were used in this study, with 20 allocated to the control group and 20 to the experimental group. After tumor implantation, all 20 mice in each group survived, with no deaths recorded during surgery or on the following day. However, at the end of the experiment, two mice died after a negligible amount of luminescence was observed in the experimental group, resulting in 18 mice in that group and 20 in the control group. Sixteen mice showed tumor growth, and four mice consistently failed to show luminescence in live imaging throughout the experiment, and no tumor growth was confirmed by H&E at the end of the experiment. The tumor growth rate was 80%.

Prominent tumor nodules detected by micro-MRI

Four weeks after tumor implantation, T2-weighted images in the sagittal and coronal planes revealed a prominent tumor nodule in the nasopharynx of the mice, presenting as a moderately hyperintense area relative to the nearby muscular and skeletal tissues, with unclear boundaries between the nodule and the surrounding tissues. The tumor size was measured in the maximum sagittal plane of the nasopharyngeal tumor, the length of which was approximately 3.90 mm, and the short diameter was ~2.42 mm (Figure 2a). Within the liver region, multiple metastatic foci exhibited high-density shadows with blurred boundaries, causing constriction of the liver tissues surrounding the nodules. All other liver tissues were normal in structure. The largest liver tumor nodule in the

maximum sagittal plane of the liver metastasis was approximately 2.39 mm long and 2.32 mm in short diameter (Figure 2b).

Histopathological and immunohistochemical analyses confirm tumor characteristics

H&E staining and immunohistochemistry confirmed the development of tumors in the nasopharynx (Figure 3a). Normal 8-week-old mice were used as negative controls. The nasal mucosal epithelium in the normal mouse was typically arranged without degeneration, necrosis, interstitial blood vessel expansion, inflammation, or tumor cells. In contrast, the tumor-bearing mice exhibited a significant mass in the nasopharynx, presenting as poorly differentiated squamous cell carcinoma, lacking an intercellular bridge, and showing abnormal keratinization and necrotic areas, with significantly atypical nuclei and cytoplasm and abnormal mitosis. Spindle cells predominated the tissue, and invasive growth destroyed normal muscle tissue and bone structure. Immunohistochemical analysis revealed the presence of CK, CK5/6, P40, and P63 in the primary tumor areas of tumor-bearing mice, with the number of proliferating cells significantly increased; conversely, no CK-, CK5/6-, P40-, and P63-positive staining was seen in the normal group (Figure 3b-e).

Several areas of metastases of varying sizes were observed in the mouse livers. In the experimental group, six mice had metastasis in the liver (rate, 30%), but no metastasis was detected in other regions. The livers of mice in the control group had neatly arranged hepatocyte cords with clearly visible hepatic sinusoids and central veins. No dilation or hyperplasia was detected in the interlobular arteries and veins or interlobular bile ducts in the portal area. In contrast, the hepatic plate and structure of the liver had disappeared in mice with liver metastases; atypical cells with poorly differentiated growth were seen, and the hepatic lobule structure was present in the tissues surrounding the tumor (Figure 4a,b).

Discussion

Progressive advances have been made in research on the progression of nasopharyngeal carcinoma, mechanisms of its progression, and treatment options. However, establishing a mouse orthotopic xenograft model of nasopharyngeal carcinoma that closely reflects the disease in clinical settings is of far-reaching significance to the continued research on nasopharyngeal carcinoma. In this study, we successfully established a dynamic observation orthotopic xenograft model of nasopharyngeal carcinoma, which facilitates the monitoring of the biological behaviors of the early-stage disease and the evaluation of the efficacies of radiotherapy, chemotherapy, and biologically targeted therapy. Hence, this new model has the potential to advance investigations on the therapeutic mechanisms associated with the treatment of nasopharyngeal carcinoma; in addition, it can aid in diagnostic imaging, interventional radiotherapy, and the targeted distribution of drugs in patients with this cancer.

C666-1-luc cells capable of persistently expressing luciferase were established by applying the lentivirus technology to

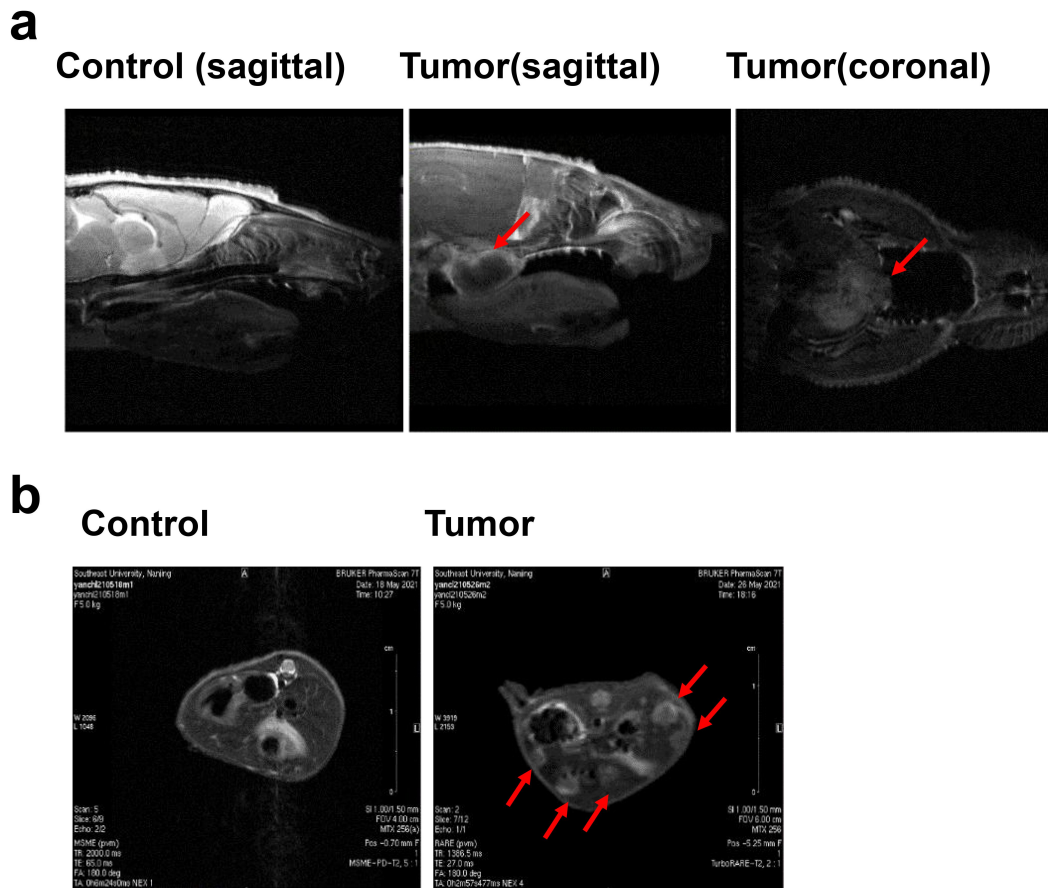


Figure 2. Prominent tumor nodules detected by micro-MRI. (a) micro-MRI of mice. Control: sagittal micro-MRI image of the nasopharynx of a normal mouse. Tumor: Coronal/sagittal micro-MRI image of the nasopharyngeal carcinoma. (b) Sagittal micro-MRI image of the mouse liver. Control: image of a section of the liver in a normal mouse. Tumor: liver of a mouse with nasopharyngeal carcinoma metastasis.

infect cells with viral vectors carrying the luciferase gene. Fluorescence images were captured by the highly sensitive *in vivo* charge-coupled device detection system when fluorescence was emitted after the injection of excessive fluorescein into the mice.³³ This method can be used to observe the biological behaviors of tumor growth, including invasion and metastasis, in a noninvasive manner and in real time.³³ Bioluminescence has low background noise and high sensitivity, without the need for exogenous excitation light, thus avoiding damage to normal cells *in vivo* during imaging. Hence, this mouse model allows for the monitoring and prediction of the progression of tumors in real-time and over the long term.^{34–36}

Animal models have long been available for developing tumors in various organs, including the lungs,^{37–39} pancreas,^{40–42} and thyroid,^{43,44} via injection of tumor cell suspensions into the orthotopic organs. Orthotopic xenograft models of these organs were developed early and rapidly and have been widely used in tumor biology and treatment research. Liu et al.⁴⁵ established nasopharyngeal carcinoma cells stably expressing GFP and injected them orthotopically into the nasopharynx to form tumors; however, the model exhibited poor reproducibility. Likewise, Smith⁴⁶ used nasopharyngeal carcinoma cells stably expressing luciferase to establish an orthotopic xenograft model of nasopharyngeal carcinoma; however, they injected the C666–1 cell suspension into the nasopharynx of mice to form tumors. The hollow nature of the

nasopharyngeal cavity makes it challenging to ensure that the liquid tumor cell suspension remains in the nasopharynx. Moreover, the cell suspensions can readily cause asphyxia, tumor spread, and even implantation metastasis to other sites, which may account, in part, for not being typically injected orthotopically into the nasopharynx for tumor formation. As an alternative, researchers often induce subcutaneous tumor formation to study the preclinical treatment schemes. For example, Qiuxia et al.⁴⁷ studied the effect of apatinib in a mouse subcutaneous tumor-bearing model of nasopharyngeal carcinoma. Likewise, to investigate the effect of a cyclin-dependent kinase inhibitor (Palbociclib) on mouse nasopharyngeal carcinoma, Hsu⁴⁸ collected tumor tissues from clinical patients to establish a mouse patient-derived xenograft (PDX) model by subcutaneous implantation into the flanks of mice. However, in subcutaneous tumor models, the tumor readily forms a capsule, grows locally, and rarely metastasizes,⁴⁹ thus limiting their capacity to demonstrate the characteristics of nasopharyngeal carcinoma, which tends to be highly aggressive and metastasizes to the liver, lungs, and bones.⁵⁰ Hence, orthotopic animal models of nasopharyngeal carcinoma require further investigation and improvement.

The tumor formation technique was improved in the present study by injecting the cell suspension subcutaneously and obtaining tissue blocks to orthotopically implant the tumor into the nasopharynx using biological glue. This method improved the tumor formation rate, reduced

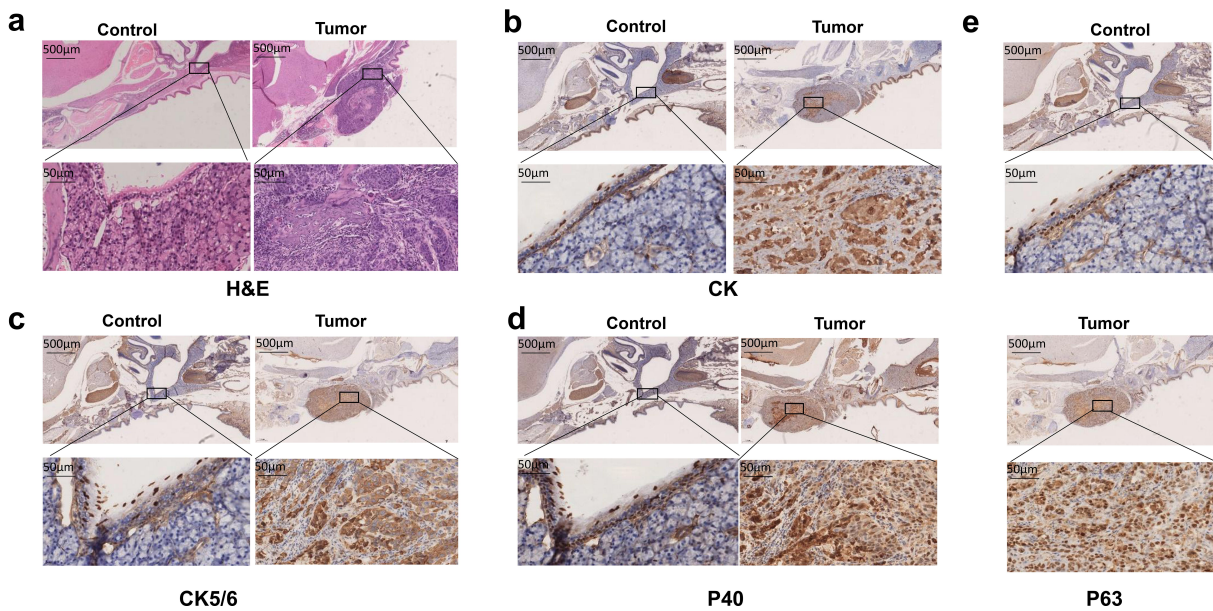


Figure 3. The tissue structure and immunohistochemical staining of the nasopharynx. (a) H&E images showed that the nasal mucosal epithelium of the normal mouse was typically arranged without degeneration, necrosis, interstitial blood vessel expansion, inflammation, or tumor cells. The tumor-bearing mice exhibited a significant mass in the nasopharynx, presenting as a poorly differentiated squamous cell carcinoma, lacking an intercellular bridge, and showing abnormal keratinization and necrotic areas, with significantly atypical nuclei and cytoplasm and abnormal mitosis. Spindle cells predominated the tissue, and invasive growth destroyed the normal muscle tissue and bone structure. (b-e) the nasopharynx of mice in the normal group were immune-negative for CK, CK5/6, P40, and P63. In the tumor-bearing mice, the primary tumor areas were positive for CK5/6 (10%), P40 (90%), CK (5%), and P63 (90%), with a significant increase in the number of proliferating cells. Magnification: 20 \times , 40 \times .

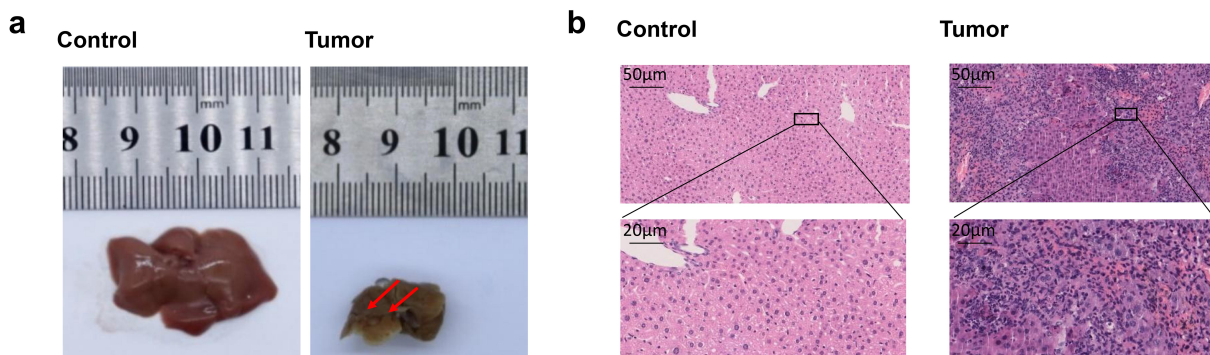


Figure 4. Gross (a) and histomorphological (b) comparisons of the mouse liver. (a) gross photograph of a normal mouse liver (control). Gross image of the liver tissue from a mouse with liver metastasis of nasopharyngeal carcinoma (tumor). (b) Control: H&E staining of a normal mouse liver. Tumor: H&E staining image of mouse with liver metastasis. Magnification: 20 \times , 40 \times . The arrow indicates the tumor site.

surgical mortality, and successfully established a mouse orthotopic xenograft model of nasopharyngeal carcinoma with good reproducibility. *In vivo* imaging technology was used to monitor tumor growth, while molecular biological techniques, such as tissue section staining and immunohistochemistry, were used to verify the tumor characteristics. This model lays the foundation for research on the pathogenesis and treatment of nasopharyngeal carcinoma and the subsequent establishment of PDX models for the individualized treatment of tumor patients. Specifically, this model closely reflects the invasion and metastatic characteristics of tumors, provides a good platform for research on nasopharyngeal carcinoma, and is more conducive to preclinical research than other tumor models.

The anatomy of the nasopharynx is complex. Early clinical symptoms of nasopharyngeal carcinoma are not typically

detected, and local invasions, such as skull base bone destruction, cavernous sinus invasion, and regular station-by-station cervical lymph node metastasis from top to bottom, can quickly occur; thus, the surgical resection of nasopharyngeal carcinoma is challenging.⁵¹ The histological classification of nasopharyngeal carcinoma includes poorly differentiated or undifferentiated carcinoma, which is sensitive to radiotherapy. With the popularization of intensity-modulated radiotherapy and the application of a comprehensive treatment, the local control rate of this disease in humans is > 90%, with a 5-year survival rate of 70%–80%.^{13,52} The demand for precise radiotherapy is increasingly important due to the extended survival time. The development of animal models promotes basic research on nasopharyngeal carcinoma and allows clinical translation and application. The current study has made innovative modifications to previous animal models, resulting in

a simple, readily produced model with stable biological characteristics that closely reflect the disease course observed in human nasopharyngeal carcinoma. In particular, the nasopharyngeal masses, structures inside and outside the cavity, and the relationship with surrounding tissues can be clearly observed via MRI, thus providing imaging evidence.

However, this new model has some limitations. First, distant metastasis could not be observed on the *in vivo* imaging system, possibly due to the small liver metastasis volumes below the detection limit. Second, traditional tumor cell suspension was

used to form the tumors rather than tumor tissues from clinical patients; hence, the model does not account for the individual heterogeneity associated with clinical cases. In addition, while our study found that tumors can be orthogonalized xenografts in the nasal region, the model may be suitable for radiation analysis in NPC, such as target volume delineation and dose distribution in normal tissue. Finally, this study focuses primarily on the establishment and validation of the orthotopic xenograft model, and a comparative analysis between the orthotopic xenograft and subcutaneous xenograft models has not been conducted. Such

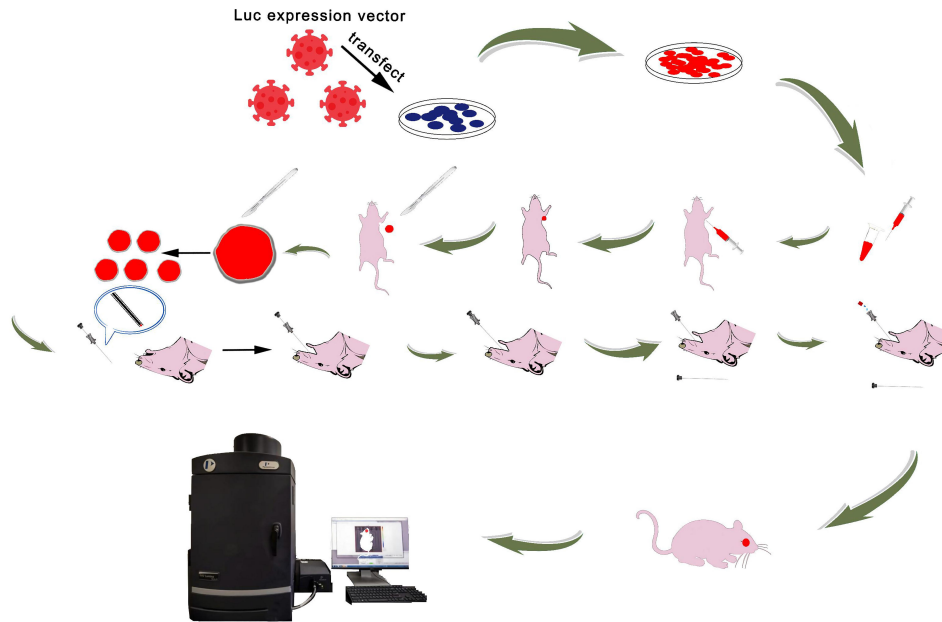


Figure 5. Schematic diagram depicting the steps in establishing an orthotopic xenograft model of nasopharyngeal carcinoma.

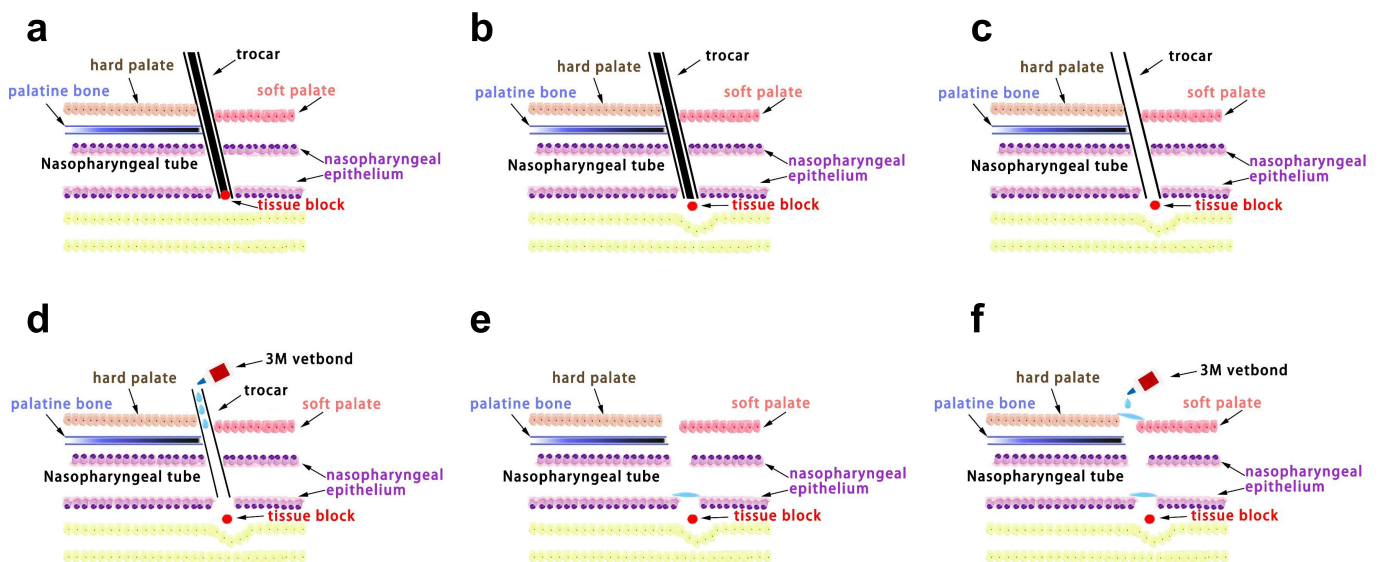


Figure 6. Anatomical schematic of the orthotopic xenograft model of nasopharyngeal carcinoma. (a) A tumor tissue block ($1 \times 1 \times 1$ mm) was inserted into the trocar and passed through the soft palate to access a position inclined to the left or right. (b) After sensing the emptiness, the nasopharynx of the nude mouse was slightly torn by picking, and the nasopharyngeal carcinoma tissue block in the cannula was pushed forward with the needle core. (c) The needle core was withdrawn. (d) An adequate amount of tissue adhesive was used to bond the inoculation port with the nasopharyngeal carcinoma tumor mass through the cannula. (e) The trocar was pulled out. (f) An adequate amount of tissue adhesive was used to adhere the bleeding point on the palate for hemostasis.

a comparative study could provide a more comprehensive understanding of the differences and similarities between the two models. This would offer valuable insights into how the tumor microenvironment influences tumor growth, metastasis, and response to treatment. Future work will include the establishment of a more intuitive and accurate PDX model of nasopharyngeal carcinoma using tumor tissue blocks from patients to better reflect the individualized clinical metastasis and disease progression process. And more about the application value of this model.

Conclusion

This study presents an ideal experimental animal model of human nasopharyngeal carcinoma with significant potential for application in research related to the growth, metastasis, prevention, and treatment of nasopharyngeal carcinoma, as well as the radiotherapy dose fractionation and drug screening for effective therapeutics.

Materials and methods

Cell culture

The Epstein – Barr virus (EBv)-positive human nasopharyngeal carcinoma cell line C666–1⁵³ was donated by the Radiation Tumor Treatment Center of the First Affiliated Hospital of Guangxi Medical University. All cells were cultured in a humidified incubator at 37°C with 5% CO₂ in RPMI medium (RPMI 1640 Medium; Gibco, CA, USA) supplemented with 10% fetal bovine serum (Gibco, CA, USA), 100 U/mL penicillin, and 50 µg/mL streptomycin (Gibco, CA, USA). Cell short tandem repeats analysis was performed to verify the characteristics of the cell line before use.

Establishment of cells stably expressing luciferase C666–1-luc

Lentiviral vectors expressing the firefly luciferase gene were purchased from Gikai Gene (Shanghai, China). Cells stably expressing luciferase C666–1-luc were obtained by transfecting the parent C666–1 cells with lentivirus carrying the firefly luciferase protein gene. At 5 days after infection, the C666–1-luc cells were selected by adding high-concentration puromycin (3 µg/mL; Gibco, CA, USA) to the cell culture for one week, after which screening was continued at a concentration of 1.5 µg/mL.

Verification of stably expressed luciferase

We confirmed luciferase expression in C666–1-luc cells by reverse transcriptase-quantitative polymerase chain reaction (RT-qPCR). Total RNA was isolated from C666–1 and C666–1-luc cells, and the RNA was reverse transcribed into cDNA by MonScript™ 5 × RTIII All-in-One Mix kit (Monad China). RT-qPCR was performed using the CFX96Touch™ system (Bio-Rad, Hercules, CA, USA) and the Monad MonAmp™ SYBR® Green qPCR Mix reverse transcription kit (Monad China). The fold change values of luciferase gene expression in the C666–1-luc cells and negative control

C666–1 cells were calculated using the $2^{-\Delta\Delta Ct}$ method. Three replicates were performed for each cDNA sample. β -actin (ACTB) was used as the internal reference. The luciferase primers were synthesized by Tsingke (Guangzhou, China), while those of β -actin were synthesized by Takara Bio (San Francisco, CA). The primer sequences were as follows: luciferase, F 5'-ATCAAAGAGGCGAACTGTGTGT -3' and R 5'-CGTCGAAGATGTTGGGGTG-3'; β -actin, F 5'-TGGCACC CAGCACAATGAA-3' and R 5'-CTAAGTCATAGTCCG CCTAGAAGCA-3'.

Additionally, *in vitro* imaging of the cells was performed. The screened C666–1-luc cells (which exhibited stable growth) and the parent cells were inoculated in 3.5 cm dishes, and 1 mL of D-fluorescein (20 mg/mL) was added to each dish. The cells were evaluated using the IVIS imaging system and quantified according to the manufacturer's instructions (PerkinElmer, China). The experiment was performed in triplicate.

Mice

Immunodeficient male BALB/C nude mice (4–6 weeks old; 12–15 g) were purchased from the Animal Experiment Centre of Guangxi Medical University. The mice were raised under specific pathogen-free (SPF) conditions and according to the protocol approved by the Animal Ethics Committee of Guangxi Medical University (201910032).

Establishment of the orthotopic xenograft Model

C666–1-luc cells (1×10^7 cells in 0.1 mL phosphate-buffered saline [PBS]) were subcutaneously injected into the right axilla of nude mice. The subcutaneous tumor was excised when the maximum diameter reached 8 mm. After removing the tissues at the outermost edge and the most central portion, the remaining tumor tissue was cut into blocks, each measuring approximately 1 mm³, and transplanted into the nasopharynx of the mice. The transplantation was performed as follows: 20 g/L pentobarbital sodium was used for intraperitoneal anesthesia (0.04 mL/g body weight); the mice were fixed on the experiment board in the supine position; a small tissue block was fixed on the puncture needle, and the mouth of the mouse was opened; the needle was inserted 5 mm inferior to the white line of the mouth at the junction of the hard and soft palate, and the tumor was implanted through the mucosa at the puncture point; 3 M Vetbond Tissue Adhesive animal tissue glue was applied dropwise to the puncture site to fix the implanted tissue. The total surgical time was approximately 5 min. No bleeding or tissue block prolapse was observed at the puncture point after the operation. After the mice awoke from anesthesia, they were returned to clean EVC cages, provided with clean feed and autoclaved water, and placed in an SPF environment for continuous feeding. The mice remained unfed for 12 h after surgery but had ad libitum access to water. The sterilized bedding, feed, and water were replaced every 3 days, and the living conditions, physical condition, and tumor growth were assessed daily. Figures 5 and 6 provide a detailed description of the experimental process and tumor implantation site.

Bioluminescence imaging

Bioluminescence imaging was performed one week after the subcutaneous and nasopharyngeal tumor implantation to verify the luminescence of the C666-1-luc cells and the growth of transplanted tumors in the mice. The growth rate and tumor size were monitored using a small animal *in vivo* imaging system twice weekly for five weeks. Briefly, each mouse was injected intraperitoneally with luciferase substrate D-luciferin (USA, sigma) at a dose of 150 mg/kg^{54,55} dissolved in sterile isotonic saline. At 15 min after the injection of D-luciferin, the mice were anesthetized with isoflurane gas (Shenzhen, China), which was maintained for the duration of the image acquisition process. Image acquisition was performed on the IVIS Lumina XRMS Series III imaging system (PerkinElmer, China) using the Living Image software (Caliper Life Sciences, Hopkinton, MA, USA). For the quantification of tumor growth kinetics, the BLI signal was measured at various time points. The ROI analysis was conducted to quantify the BLI signal in photons per second (p/s).

Magnetic resonance imaging (MRI)

A 7.0 T micro-MRI system with a four-channel phased array surface coil (Bruker, Pharmacan) was used to perform micro-MRI scans of the nasopharyngeal carcinoma in the mice and record the tumor locations and measurements. During examination, the mice were fixed on the scaffold in the prone position and anesthetized with 1.5% isoflurane. All images were acquired in the transverse plane using the TurboRARE-T2 weighted sequence (repetition time msec/echo time msec, 3000/45; one signal acquired; matrix of 256 × 256 applied with a section thickness of 1 mm; and a flip angle of 180°). The field of view was 20 × 16 mm, with 13 layers and a maximum resolution of 62 μm.

Histological evaluation and immunohistochemistry

The mice were euthanized after *in vivo* imaging and micro-MRI imaging. The head and liver tissues of the mice were completely removed, fixed with 4% paraformaldehyde for 24 h, and then embedded in paraffin blocks (the head tissues were subjected to bone decalcification with EDTA for more than 4 weeks). The paraffin blocks were cut into 4-μm-thick continuous sections, and some were stained with hematoxylin and eosin (H&E). The pathological features of the tissues were observed by light microscopy to confirm the presence of nasopharyngeal tumors and liver metastases, as well as the pathological type and invasion scope of the tumor. Some sections were stained with CK (Leica, Cat# NCL-AE1/AE3), CK5/6 (Leica, Cat# NCL-L-CK5/6), P40 (CELVNTE, Cat# CPM-0133), and P63 (DAKO, Cat# M7317) for immunohistochemical analysis. After dewaxing and hydration, the sections were soaked in 0.01 M citrate buffer, heated, and incubated at 95 °C–98°C for 10 min. The sections were then slowly cooled to room temperature, incubated with an endogenous peroxidase blocker at 37°C for 10 min, and blocked with 5% BSA at 37°C for 30 min. The primary antibodies were diluted with antibody dilution buffer containing 1% bovine serum albumin and 0.3% Triton

X-100 in 1X PBS, and the slides were incubated at 4°C overnight. Following restoration to room temperature, the slides were washed with PBS thrice, incubated with a secondary antibody (Leica, Cat# RE7280-K) at room temperature in the dark for 1 h, stained with DAB and hematoxylin, and gently washed in water for 10 min. The slides were sealed with neutral resin after being soaked in xylene for 5 minutes. After staining, the local morphological characteristics of the tumor cells were observed under an inverted microscope, and images were captured with a NanoZoomer S60 (Hamamatsu, Japan) digital slide scanner. The gross features, location, and invasive properties of the local tumor were comprehensively observed, and images were analyzed using the NDP View 2 software.

Statistical analysis

All data are expressed as mean ± standard deviation (SD). Students' t-tests were used to compare inter-group differences. All analyses were carried out using the GraphPad Prism software (Version 6.01, USA), and the results were considered statistically significant when the P-value was < 0.05.

Acknowledgments

This manuscript has been preprinted (www.researchsquare.com/article/rs-2029538/v1). Our article has been published on Journal of Clinical Oncology as a Meeting Abstract and the manuscript has been derived from the meeting abstract (https://ascopubs.org/doi/abs/10.1200/JCO.2022.40.16_suppl.e18048).

Disclosure statement

No potential conflict of interest was reported by the authors.

Funding

This work was supported by grants from the National Natural Science Foundation of China [No. 82272736, 82160467, 81460460 and 81760542], The Research Foundation of the Science and Technology Department of Guangxi Province, China [grant No. 2023GXNSFDA026009, 2016GXNSFAA380252, 2018AB61001 and 2014GXNSFBA118114], the Research Foundation of the Health Department of Guangxi Province, China [No. S2018087], Guangxi Medical University Training Program for Distinguished Young Scholars (2017), Medical Excellence Award Funded by the Creative Research Development Grant from the First Affiliated Hospital of Guangxi Medical University (2016). Guangxi Medical High-level Talents Training Program. The central government guide local science and technology development projects [ZY18057006].

ORCID

Wei Chen  <http://orcid.org/0000-0001-8211-7963>

Authors' contributions

MK designed the study. WC, SC, LJ, SL, ZZ, M S, YY, YQ, CY, XS, and WC helped with the experiments. MK, WC and SC analyzed the experimental data

Availability of data and materials

All data generated or analyzed during this study are included in this published article.

Competing interests

The authors have no competing interest to declare.

Consent for publication

Not applicable.

Ethics approval and consent to participate

The study was approved by the Animal Ethics Committee of Guangxi Medical University (Approval # 201910032). All mice were used in accordance with the National Policy and Regulations on Use of Laboratory Animals. All animal experiments were carried out in compliance Animal Research: Reporting of In Vivo Experiments (ARRIVE) guidelines.

References

- Chen Y-P, Chan ATC, Le Q-T, Blanchard P, Sun Y, Ma J. Nasopharyngeal carcinoma. *Lancet*. 2019;394(10192):64–80. doi:10.1016/S0140-6736(19)30956-0.
- Chua MLK, Wee JTS, Hui EP, Chan ATC. Nasopharyngeal carcinoma. *Lancet*. 2016;387(10022):1012–24. doi:10.1016/S0140-6736(15)00055-0.
- Cao S-M, Simons MJ, Qian C-N. The prevalence and prevention of nasopharyngeal carcinoma in China. *Chin J Cancer*. 2011;30(2):114–19. doi:10.5732/cjc.010.10377.
- Jia W-H, Huang Q-H, Liao J, Ye W, Shugart YY, Liu Q, Chen L-Z, Li Y-H, Lin X, Wen F-L et al. Trends in incidence and mortality of nasopharyngeal carcinoma over a 20–25 year period (1978/1983–2002) in Sihui and Cangwu counties in southern China. *BMC Cancer*. 2006;6(1):178. doi:10.1186/1471-2407-6-178.
- Ferlay J, Ervik M, Lam F, Colombet M, Mery L, Piñeros M, Znaor A, Soerjomataram I, Bray F. Global cancer observatory: cancer Today. Lyon, France: International Agency for Research on Cancer. [accessed 2021 Sep 16]. <https://gco.iarc.who.int/today>.
- Wt F, Ym Y, Yl B, W Q. Diversity of intestinal microflora in patients with depression after stroke. *Nan Fang Yi Ke Da Xue Xue Bao*. 2016;10:1305–11.
- Wong KCW, Hui EP, Lo K-W, Lam WKJ, Johnson D, Li L, Tao Q, Chan KCA, To K-F, King AD. et al. Nasopharyngeal carcinoma: an evolving paradigm. *Nat Rev Clin Oncol*. 2021;18(11):679–95. doi:10.1038/s41571-021-00524-x.
- Carioli G, Negri E, Kawakita D, Garavello W, La Vecchia C, Malvezzi M. Global trends in nasopharyngeal cancer mortality since 1970 and predictions for 2020: focus on low-risk areas. *Int J Cancer*. 2017;140(10):2256–64. doi:10.1002/ijc.30660.
- Liebowitz D. Nasopharyngeal carcinoma: the Epstein-Barr virus association. *Semin Oncol*. 1994;21(3):376–81.
- Chua ML, Sun Y, Supiot S. Advances in nasopharyngeal carcinoma — “west meets east”. *Br J Radiol*. 2019;92(1102):20199004–. doi:10.1259/bjr.20199004.
- Tan W-L, Tan E-H, Lim D-T, Ng Q-S, Tan D-W, Jain A, Ang M-K. Advances in systemic treatment for nasopharyngeal carcinoma. *Chin Clin Oncol*. 2016;5(2):21. doi:10.21037/cco.2016.03.03.
- Lee AWM, Sze WM, Au JSK, Leung SF, Leung TW, Chua DTT, Zee BCY, Law SCK, Teo PML, Tung SY. et al. Treatment results for nasopharyngeal carcinoma in the modern era: the Hong Kong experience. *Int J Radiat Oncol Biol Phys*. 2005;61(4):1107–16. doi:10.1016/j.ijrobp.2004.07.702.
- Blanchard P, Lee A, Marguet S, Leclercq J, Ng WT, Ma J, Chan ATC, Huang P-Y, Benhamou E, Zhu G. et al. Chemotherapy and radiotherapy in nasopharyngeal carcinoma: an update of the MAC-NPC meta-analysis. *Lancet Oncol*. 2015;16(6):645–55. doi:10.1016/S1470-2045(15)70126-9.
- Chan OSH, Ngan RKC. Individualized treatment in stage IVC nasopharyngeal carcinoma. *Oral Oncol*. 2014;50(9):791–97. doi:10.1016/j.oraloncology.2014.01.004.
- Mendenhall WM, Amdur RJ, Palta JR. Intensity-modulated radiotherapy in the standard management of head and neck cancer: promises and pitfalls. *J Clin Oncol*. 2006;24(17):2618–23. doi:10.1200/JCO.2005.04.7225.
- Tan Z, Xiao L, Tang M, Bai F, Li J, Li L, Shi F, Li N, Li Y, Du Q. et al. Targeting CPT1A-mediated fatty acid oxidation sensitizes nasopharyngeal carcinoma to radiation therapy. *Theranostics*. 2018;8(9):2329–47. doi:10.7150/thno.21451.
- Liu F, Pan Q, Wang L, Yi S, Liu P, Huang W. Anticancer targets and mechanisms of calycosin to treat nasopharyngeal carcinoma. *Biofactors*. 2020;46(4):675–84. doi:10.1002/biof.1639.
- Zhang P, He Q, Lei Y, Li Y, Wen X, Hong M, Zhang J, Ren X, Wang Y, Yang X. et al. mA-mediated ZNF750 repression facilitates nasopharyngeal carcinoma progression. *Cell Death Dis*. 2018;9(12):1169. doi:10.1038/s41419-018-1224-3.
- Wang T, Du M, Zhang W, Bai H, Yin L, Chen W, He X, Chen Q. MicroRNA-432 suppresses invasion and migration via E2F3 in nasopharyngeal carcinoma. *Onco Targets Ther*. 2019;12:11271–80. doi:10.2147/OTT.S233435.
- Khanna C, Hunter K. Modeling metastasis in vivo. *Carcinogenesis*. 2005;26(3):513–23. doi:10.1093/carcin/bgh261.
- Ahmad A, Stefani S. Distant metastases of nasopharyngeal carcinoma: a study of 256 male patients. *J Surg Oncol*. 1986;33(3):194–97. doi:10.1002/jso.2930330310.
- Dubrulle F, Souillard R, Hermans R. Extension patterns of nasopharyngeal carcinoma. *Eur Radiol*. 2007;17(10):2622–30. doi:10.1007/s00330-007-0616-z.
- Hoffman RM. Orthotopic metastatic mouse models for anticancer drug discovery and evaluation: a bridge to the clinic. *Invest New Drugs*. 1999;17(4):343–59. doi:10.1023/A:1006326203858.
- Kim S. Animal models of cancer in the head and neck region. *Clin Exp Otorhinolaryngol*. 2009;2(2):55–60. doi:10.3342/ceo.2009.2.2.55.
- Kellar A, Egan C, Morris D. Preclinical murine models for lung cancer: clinical trial applications. *Biomed Res Int*. 2015;2015:621324. doi:10.1155/2015/621324.
- Greco A, Auletta L, Orlandella FM, Iervolino PLC, Klain M, Salvatore G, Mancini M. Preclinical imaging for the study of mouse models of thyroid cancer. *IJMS*. 2017;18(12):18. doi:10.3390/ijms18122731.
- Kocher B, Piwnicka-Worms D. Illuminating cancer systems with genetically engineered mouse models and coupled luciferase reporters in vivo. *Cancer Discov*. 2013;3(6):616–29. doi:10.1158/2159-8290.CD-12-0503.
- Bimonte S, Barbieri A, Palma G, Luciano A, Rea D, Arra C. Curcumin inhibits tumor growth and angiogenesis in an orthotopic model of human pancreatic cancer. *Biomed Res Int*. 2013;2013:810423. doi:10.1155/2013/810423.
- Wang K, Jin W, Jin P, Fei X, Wang X, Chen X. miR-211-5p suppresses metastatic behavior by targeting SNAIL1 in renal cancer. *Mol Cancer Res*. 2017;15(4):448–56. doi:10.1158/1541-7786.MCR-16-0288.
- Wu T, Heuillard E, Lindner V, Bou About G, Ignat M, Dillenseger J-P, Anton N, Dalimier E, Gossé F, Fouré G. et al. Multimodal imaging of a humanized orthotopic model of hepatocellular carcinoma in immunodeficient mice. *Sci Rep*. 2016;6(1):35230. doi:10.1038/srep35230.
- Shankar S, Ganapathy S, Srivastava RK. Sulforaphane enhances the therapeutic potential of TRAIL in prostate cancer orthotopic model through regulation of apoptosis, metastasis, and angiogenesis. *Clin Cancer Res*. 2008;14(21):6855–66. doi:10.1158/1078-0432.CCR-08-0903.

32. Gosnell H, Kasman LM, Potta T, Vu L, Garrett-Mayer E, Rege K, Voelkel-Johnson C. Polymer-enhanced delivery increases adenoviral gene expression in an orthotopic model of bladder cancer. *J Control Release*. 2014;176:35–43. doi:10.1016/j.jconrel.2013.12.012.
33. Wu JC, Sundaresan G, Iyer M, Gambhir SS. Noninvasive optical imaging of firefly luciferase reporter gene expression in skeletal muscles of living mice. *Mol Ther*. 2001;4(4):297–306. doi:10.1006/mthe.2001.0460.
34. Keyaerts M, Cavelliers V, Lahoutte T. Bioluminescence imaging: looking beyond the light. *Trends Mol Med*. 2012;18(3):164–72. doi:10.1016/j.molmed.2012.01.005.
35. Lim E, Modi KD, Kim J. In vivo bioluminescent imaging of mammary tumors using IVIS spectrum. *J Vis Exp*. 2009; doi:10.3791/1210-v.
36. Zinn KR, Chaudhuri TR, Szafran AA, O'Quinn D, Weaver C, Dugger K, Lamar D, Kesterson RA, Wang X, Frank SJ. et al. Noninvasive bioluminescence imaging in small animals. *Ilar J*. 2008;49(1):103–15. doi:10.1093/ilar.49.1.103.
37. Jarry U, Bostoën M, Pineau R, Chaillot L, Mennessier V, Montagne P, Motte E, Gournay M, Le Goff A, Guillaudeux T. et al. Orthotopic model of lung cancer: isolation of bone micro-metastases after tumor escape from osimertinib treatment. *BMC Cancer*. 2021;21(1):530. doi:10.1186/s12885-021-08205-9.
38. Chen X, Su Y, Fingleton B, Acuff H, Matrisian LM, Zent R, Pozzi A. An orthotopic Model of lung cancer to analyze primary and metastatic NSCLC growth in integrin $\alpha 1$ -null mice. *Clin Exp Metastasis*. 2005;22(2):185–93. doi:10.1007/s10585-005-7453-8.
39. Gagnadoux F, Pape AL, Lemarié E, Lerondel S, Valo I, Leblond V, Racineux JL, Urban T. Aerosol delivery of chemotherapy in an orthotopic model of lung cancer. *Eur Respir J*. 2005;26(4):657–61. doi:10.1183/09031936.05.00017305.
40. Lewis CS, Karve A, Matiash K, Stone T, Li J, Wang JK, Versteeg HH, Aronow BJ, Ahmad SA, Desai PB. et al. A first-in-class, humanized antibody targeting alternatively spliced tissue factor: preclinical evaluation in an orthotopic Model of pancreatic ductal adenocarcinoma. *Front Oncol*. 2021;11:691685. doi:10.3389/fonc.2021.691685.
41. Tseng WW, Winer D, Kenkel JA, Choi O, Shain AH, Pollack JR, French R, Lowy AM, Engleman EG. Development of an orthotopic model of invasive pancreatic cancer in an immunocompetent murine host. *Clin Cancer Res*. 2010;16(14):3684–95. doi:10.1158/1078-0432.CCR-09-2384.
42. Li L, Yue GGL, Fung KP, Leung PC, Lau CBS, Leung PS. Establishment of an orthotopic model of pancreatic cancer to evaluate the antitumor effects of irinotecan through the biomarker carbohydrate antigen 19-9 in mice. *Pancreas*. 2014;43(7):1126–28. doi:10.1097/MPA.000000000000183.
43. Kim S, Park Y-W, Schiff BA, Doan DD, Yazici Y, Jasser SA, Younes M, Mandal M, Bekele BN, Myers JN. et al. An orthotopic model of anaplastic thyroid carcinoma in athymic nude mice. *Clin Cancer Res*. 2005;11(5):1713–21. doi:10.1158/1078-0432.CCR-04-1908.
44. Oweida A, Phan A, Vancourt B, Robin T, Hararah MK, Bhatia S, Milner D, Lennon S, Pike L, Raben D. et al. Hypofractionated radiotherapy is Superior to conventional fractionation in an Orthotopic Model of anaplastic thyroid cancer. *Thyroid*. 2018;28(6):739–47. doi:10.1089/thy.2017.0706.
45. Liu T, Ding Y, Xie W, Li Z, Bai X, Li X, Fang W, Ren C, Wang S, Hoffman RM. et al. An imageable metastatic treatment model of nasopharyngeal carcinoma. *Clin Cancer Res*. 2007;13(13):3960–67. doi:10.1158/1078-0432.CCR-07-0089.
46. Smith PA, Merritt D, Barr L, Thorley-Lawson DA. An orthotopic model of metastatic nasopharyngeal carcinoma and its application in elucidating a therapeutic target that inhibits metastasis. *Genes & Cancer*. 2011;2(11):1023–33. doi:10.1177/1947601912440878.
47. Peng Q-X, Han Y-W, Zhang Y-L, Hu J, Fan J, Fu S-Z, Xu S, Wan Q. Apatinib inhibits VEGFR-2 and angiogenesis in an in vivo murine model of nasopharyngeal carcinoma. *Oncotarget*. 2017;8(32):52813–22. doi:10.18632/oncotarget.17264.
48. Hsu C-L, Lui K-W, Chi L-M, Kuo Y-C, Chao Y-K, Yeh C-N, Lee L-Y, Huang Y, Lin T-L, Huang M-Y. et al. Integrated genomic analyses in PDX model reveal a cyclin-dependent kinase inhibitor palbociclib as a novel candidate drug for nasopharyngeal carcinoma. *J Exp Clin Cancer Res*. 2018;37(1):233. doi:10.1186/s13046-018-0873-5.
49. Sharkey FE, Fogh J. Metastasis of human tumors in athymic nude mice. *Int J Cancer*. 1979;24(6):733–38. doi:10.1002/ijc.2910240605.
50. Zou X, You R, Liu H, He Y-X, Xie G-F, Xie Z-H, Li J-B, Jiang R, Liu L-Z, Li L. et al. Establishment and validation of M1 stage subdivisions for de novo metastatic nasopharyngeal carcinoma to better predict prognosis and guide treatment. *Eur J Cancer*. 2017;77:117–26. doi:10.1016/j.ejca.2017.02.029.
51. Wei WI, Sham JST. Nasopharyngeal carcinoma. *Lancet*. 2005;365(9476):2041–54. doi:10.1016/S0140-6736(05)66698-6.
52. Tham I-K, Hee SW, Yeo R-C, Salleh PB, Lee J, Tan T-K, Fong KW, Chua ET, Wee JTS. Treatment of nasopharyngeal carcinoma using intensity-modulated radiotherapy—the national cancer centre Singapore experience. *Int J Radiat Oncol Biol Phys*. 2009;75(5):1481–86. doi:10.1016/j.ijrobp.2009.01.018.
53. Cheung ST, Huang DP, Hui AB, Lo KW, Ko CW, Tsang YS, Wong N, Whitney BM, Lee JCK. Nasopharyngeal carcinoma cell line (C666-1) consistently harbouring Epstein-Barr virus. *Int J Cancer*. 1999;83(1):121–26. doi:10.1002/(SICI)1097-0215.
54. Li H-W, Li J, Helm GA, Pan D. Highly specific expression of luciferase gene in lungs of naïve nude mice directed by prostate-specific antigen promoter. *Biochem Biophys Res Commun*. 2005;334(4):1287–91. doi:10.1016/j.bbrc.2005.07.025.
55. Tuli R, Surmak A, Reyes J, Hacker-Prietz A, Armour M, Leubner A, Blackford A, Tryggstad E, Jaffee EM, Wong J. et al. Development of a novel preclinical pancreatic cancer research model: bioluminescence image-guided focal irradiation and tumor monitoring of orthotopic xenografts. *Transl Oncol*. 2012;5(2):77–84. doi:10.1593/tlo.11316.